ACS OMEGA

http://pubs.acs.org/journal/acsodf

Article

Luminescent MoS_2 Quantum Dots with Tunable Operating Potential for Energy-Enhanced Aqueous Supercapacitors

Sarojini Jeeva Panchu, Kumar Raju,* Hendrik C. Swart, Bharatiraja Chokkalingam, Malik Maaza, Mohamed Henini, and Mathew K. Moodley*

Cite This: *ACS Omega* 2021, 6, 4542−4550

Read Online

ACCESS | Metrics & More | Article Recommendations | Supporting Information

ABSTRACT: Wide band gap luminescent MoS_2 quantum dots (QDs) and MoS_2 nanocrystals (NCs) have been synthesized by using laser-assisted chemical vapour deposition and used as an electrode material in supercapacitors. Size-dependent properties of the MoS_2 QDs and NCs were examined by UV−vis absorption, photoluminescence, and Raman spectroscopy. The morphological evolution of the NCs and QDs were characterized by using field emission scanning electron microscopy, high-resolution transmission electron microscopy, and atomic force microscopy. The as-synthesized uniform QDs with a size of ∼2 nm exhibited an extended electrochemical potential window of 0.9 V with a specific capacitance value of 255 F/g, while the NCs values were 205 F/g and 0.8 V and the pristine MoS_2 with values of 105 F/g and 0.6 V at a scan rate of 1 mV s^{-1}. A shorter conductive pathway and 3D quantum confinement of MoS_2 QDs that exhibited a higher number of active sites ensure that the efficient charge storage kinetics along with the intercalation processes at the available edge sites enable significant widening of operating potential window and enhance the capacitance. The symmetric device constructed with the QDs showed a remarkable device capacitance of 50 F/g at a scan rate of 1 mV s^{-1} with an energy density of ∼5.7 W h kg^{-1} and achieved an excellent cycle stability of 10,000 consecutive cycles with ∼95% capacitance retention.

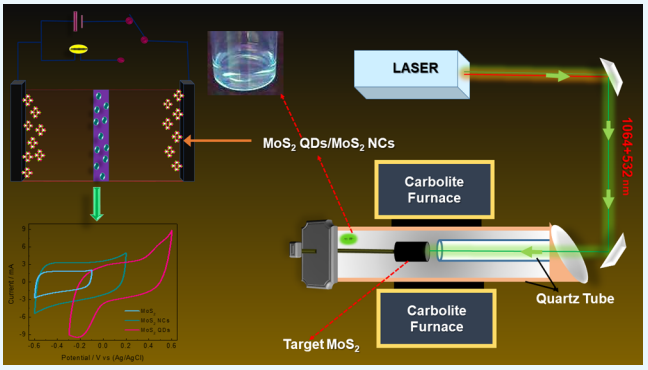

INTRODUCTION

Supercapacitors (SCs) have attracted huge attention in the recent years because of their intermediate electrochemical performance between the electrochemical double-layer capacitors and lithium-ion batteries.[1−3] Although the non-aqueous electrolytes, namely, organic and ionic liquid-based electrolytes, with wider working voltage window benefit the SCs with high energy densities, the critical bottlenecks of low ionic conductivity, flammability, and toxicity require optimal condition for operation which remains critical when compared to aqueous SCs. Aqueous electrolytes possess superior advantages of high ionic conductivity (∼1 S cm^{-1}) safe, easy to handle, and inexpensive and offer the potential for storing a large amount of charges. However, one of the main critical challenges of SCs is the lower energy density in comparison with lithium-ion batteries.[4] Thus, new materials are being sought to overcome this challenge. The 2D materials such as MoS_2, graphene, metal phosphates, and MXene-based SC devices are promising for realizing the high energy density to some extent.[5−9] In the case of MoS_2, the unique atomic structure with S−Mo−S atomic layers analogue to the graphene-like structure has gained massive attraction because of its ability to be synthesized with various structural configurations but yet maintains a layered structure.[10,11] To achieve substantial electrochemical performances, it is critical for the transport of electrons and ions in a shorter diffusion lengths.[12,13] Numerous studies on the structural and topological changes with tunable physicochemical properties of MoS_2 by various synthesis methods have been reported.[14,15]

A binder-free vertically grown MoS_2 nanosheet prepared by the hydrothermal method was utilized as a flexible electrode that shows a capacitance value of 2236.6 mF cm^{-2} and a cycle stability of 86.1% when 2000 cycles.[16] A MoS_2/CNT nanocomposite-based SC shows a capacity value of 74.05 F/g.[17] Wang et al. prepared the nanocomposite of MoS_2 nanosheets with a Bi_2S_3 nanorod-based electrode for SC that shows a specific capacitance value of 120.2 F g^{-1}. The cycle stability was 87.7% after 2000 cycles.[18] An electrode material prepared by the composite of the carbon−MoS_2 hierarchical

Received: August 26, 2020
Accepted: November 18, 2020
Published: February 11, 2021

https://dx.doi.org/10.1021/acsomega.0c02576
ACS Omega 2021, 6, 4542−4550

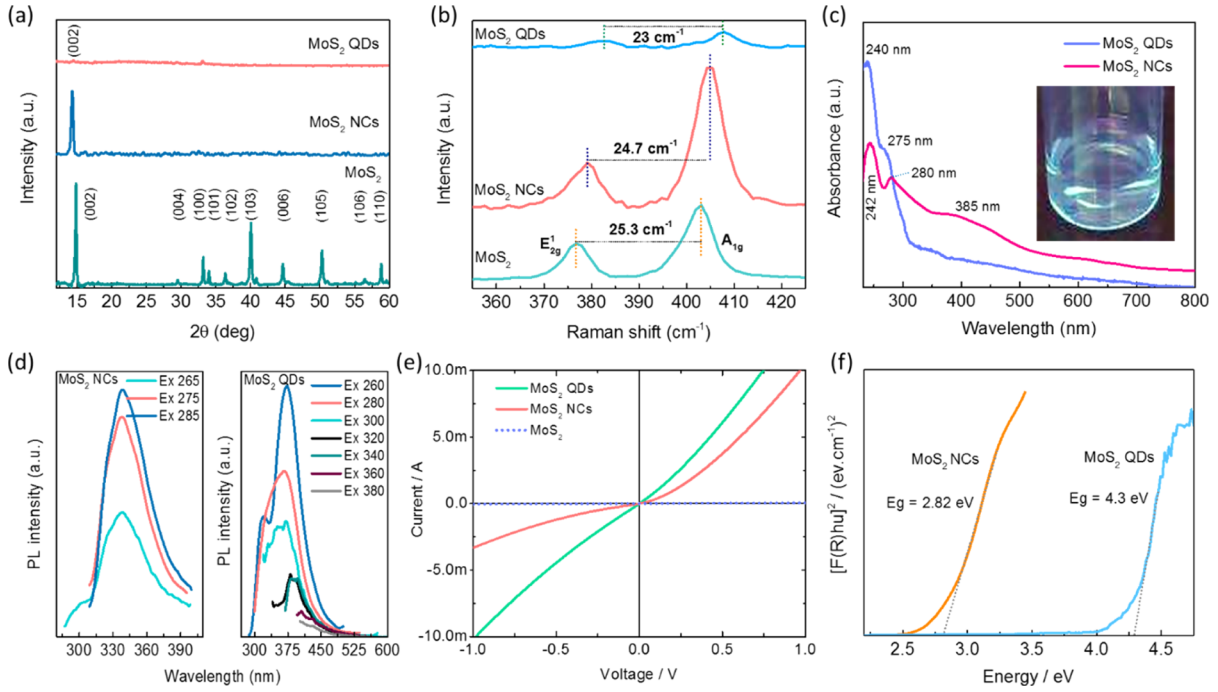

Figure 1. Physical characterisation of bulk MoS_2, MoS_2 NCs, and MoS_2 QDs. (a) XRD patterns with their corresponding lattice reflections, (b) Raman spectra with frequency differences, (c) UV, (d) luminescence, (e) conductivity, and (f) band gap.

microsphere shows a capacitance of 120 F g^{-1} over 3000 cycles.[19] A nanocomposite material by using flower like MoS_2 grown on carbon nanosheets exhibits the specific capacitance 381 F/g and the 92% capacitance retention after 3000 cycles.[20] Furthermore, various forms of MoS_2 nanomaterial such as oxygen−MoS_2 microspheres,[21] 1T-MoS_2 nanosheets,[22,23] MoS_2/rGO decorated NiO,[24] and Ni_xS_y/MoS_2[25] served as an electrode material for the SC devices.

The quantum dots (QDs) in the range of 2−10 nm in diameters highlighted the efficient and stable quantum confinement effects which strongly assists the excellent physical and chemical properties.[26−28] Besides, the larger surface to volume ratio, the higher concentration of edge atoms, and size effects of QDs have significantly contributed to the enhancement of charge transportation when compared to the MoS_2 monolayers and bulk MoS_2.[29,30] Furthermore, the luminescent electrode materials, especially MoS_2 QDs with 3D quantum confinement showing a higher number of active sites responsible for efficient charge storage kinetics and also the intercalation processes at the available edges enable significant widening of operating potential window and enhance the capacitance. However, achieving uniform QDs with narrow size distributions remains a critical challenge.

There has been significant evidence of synthesizing uniform MoS_2 QDs.[31−36] Despite the advantages of synthesis methods reported, the structural destruction and harsh chemical treatments, especially, the introduction of metallic heteroatoms by chemical intercalation, the formation of byproducts by complex chemical treatments and restacking of monolayers remain a bottleneck for making uniform MoS_2 QDs.

Here, we report on the laser assisted chemical vapor deposition (LACVD) for the synthesizing of wide band gap luminescent MoS_2 QDs and nanocrystals (NCs) with uniform size distribution. This material was further used as an electrode material for SCs. It was shown that the induced defects as a result of edge and size effects of the MoS_2 QDs enhanced the active sites responsible for efficient charge accumulations.[29] Pan and Zhang reported that MoS_2 may exhibit the favorable electrochemical performance by its twofold ability of charge accumulation at the interspace of layers as double layers and faradaic redox reactions at its dangling edge structure.[37] Furthermore, Li et al. reported that the performances are also highly dependent on the crystalline nature, phase, layer numbers, as well as the lateral size of the sheets.[29] As such, here, we investigated the charge separation efficiency, redox active sites, and intercalation phenomena of the MoS_2 QDs, NCs, as well as bulk MoS_2 and determining their electrochemical properties and potential use as SCs.

RESULTS AND DISCUSSION

Figure 1a compares the X-ray diffraction (XRD) patterns obtained from the bulk MoS_2, MoS_2 NCs and MoS_2 QDs which shows the highly crystalline nature with characteristic sharp peaks obtained for bulk and NCs of MoS_2. The diffraction patterns are well matched and indexed according to the ICDD pattern no. 00-037-1492, which indicate the presence of the 2H-MoS_2 phase. More importantly, no peaks were noticed from gold (Au) which was used in low concentration as a catalyst for the synthesis of the MoS_2. The most intense peak is located at 14.3° and corresponds to the (002) reflection with lattice expansion of the S−Mo−S toward lower 2θ indicating the formation of a few layers of MoS_2 NCs. A very weak peak at 14.3° of the (002) reflection for the QDs shows weaker interlayer interactions, which strongly validate the presence of mono or bilayers of the MoS_2 QDs. The number of layers of the as-synthesized MoS_2 NCs and QDs were also confirmed by Raman spectroscopy, and the spectra are shown in Figure 1b. The spectrum for MoS_2 reveals the signature in-plane E^1_{2g} the vibration of Mo and S atoms and out-of-plane A_{1g} the vibration of S atoms at 404.5 and 379.8 cm^{-1} for the NCs and 406 and 383 cm^{-1} for the QDs, respectively.[38]

https://dx.doi.org/10.1021/acsomega.0c02576
ACS Omega 2021, 6, 4542−4550

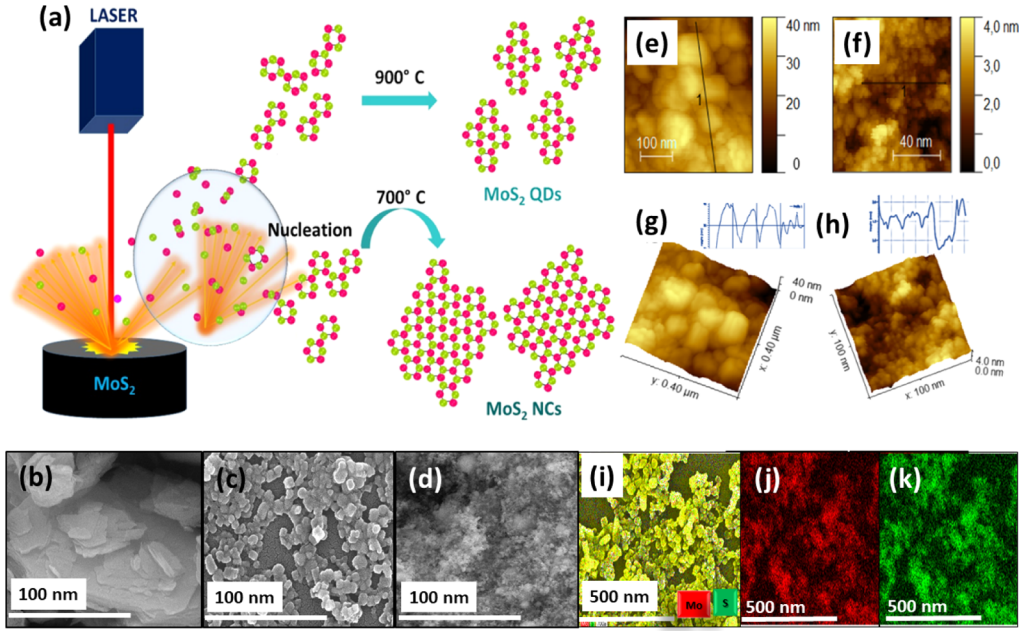

Figure 2. (a) Schematic representation of MoS_2 NCs and QDs formation from laser-induced plasma. (b–d) FESEM of bulk MoS_2, MoS_2 NCs, atomic force microscopy (AFM) analysis of MoS_2 NCs (e,g) and QDs (f,h), and the elemental mapping of MoS_2 NCs (i) Mo (red) (j) and S (green) (k).

In comparison with bulk MoS_2 (25.3 cm^{-1}), a blue shift related to the E^1_{2g} and A_{1g} vibrations is realized, and the frequency difference between the vibrations was calculated to be 24.7 and 23 cm^{-1} for the NCs and QDs, respectively, suggesting weakened interlayer interactions that further probe the existence of a few layers of the NCs and QDs with a 1–3 layered nanosheets.[29,39] UV–vis absorption analysis was further used to investigate the lateral dimensions of the nanosheets (Figure 1c).

Typical absorption bands were observed at 242, 280, 385, 617, and 667 nm for the MoS_2 NCs. The low energy bands at ~617 and ~667 nm correspond to the *k*-point of the Brillouin zone for the MoS_2 NCs whereas the peaks emerge at 242 and 280 nm due to the *M*-point of the Brillouin zone of the direct transition from the deep valence band to the conduction band. Excitingly, the MoS_2 QDs exhibited only two high energy absorption peaks near the UV region at 240 and 275 nm which are attributed to the direct transition from the deep valence band to the conduction band, and the bands are strongly blue shifted due to the confinement and edge effects which infer that the QDs are with the lateral size of >50 nm.

The luminescent properties of the QDs were analyzed by using photoluminescence (PL) spectroscopy. The aqueous solution of the MoS_2 QDs emitted blue light under UV irradiation at a wavelength of 365 nm, as depicted in Figure 1d.[40] The PL spectra of the MoS_2 QDs at room temperature under various excitation wavelengths show that the dominant PL peak shifted toward longer wavelengths as the excitation wavelength was increased above 300–360 nm. The emission peak continued to shift toward the red with increasing excitation wavelength, but with rapidly decreasing intensity. The strong excitation-dependent emission spectra are attributed to the polydispersity and the hot PL from the *k*-point of the Brillouin zone of the surfaces of the MoS_2 QDs.

The four-point probe method was used to measure the electrical resistivity of the samples. The applied bias-voltage range of −1 to 1 V are given in Figure 1e. Application of the external bias increased the current significantly for the NCs and QDs, reflecting Ohmic-like characteristics.

$$R_{sh} = \frac{\rho}{t} = \frac{\pi}{\ln(2)}\frac{V}{I} \quad (1)$$

where R is the sheet resistance, ρ is the resistivity, t is the thickness of the film, V is the applied voltage and I is the measured current. The conductivity (σ) of the samples are calculated by using the formula, ($\sigma = 1/\rho$). The calculated resistivity and conductivity of the as-synthesized samples are listed in Table S1 (Supporting Information). Based on the quantum confinement effect on the as-synthesized MoS_2 NCs and QDs, the electrical conductivity changed. The electron flow is restricted in NCs compared to QDs, thus the electrical conductivity is lower for NCs. The electrical conductivity for MoS_2 QDs showed good electron conductivity between the layers, so it showed less resistivity. The as-synthesized MoS_2 QDs showed an electrical conductivity of 268.46 S/cm owing to the zero-dimensional growth with good crystallinity of the QDs.

The optical band gap energy was calculated by the Kubelka–Munk equation, which is based on the transformation of diffuse reflectance measurements to estimate band gap values with good accuracy

$$F(R) = \frac{(1-R)^2}{2 \times R} = \frac{k}{s} \quad (2)$$

where $F(R)$ is the Kubelka–Munk function, R is the reflectance, k is the molar absorption coefficient, and s is the scattering coefficient. The band gap is calculated by using the following Kubelka–Munk equation, as indicated in eq 3

$$[F(R)h\nu] = A(h\nu - E_g)^n \quad (3)$$

where A is the proportionality constant, $h\nu$ is the photon energy, and E_g is the optical band gap, and n is a constant associated with different kinds of electronic transitions ($n = 1/$

https://dx.doi.org/10.1021/acsomega.0c02576
ACS Omega 2021, 6, 4542–4550

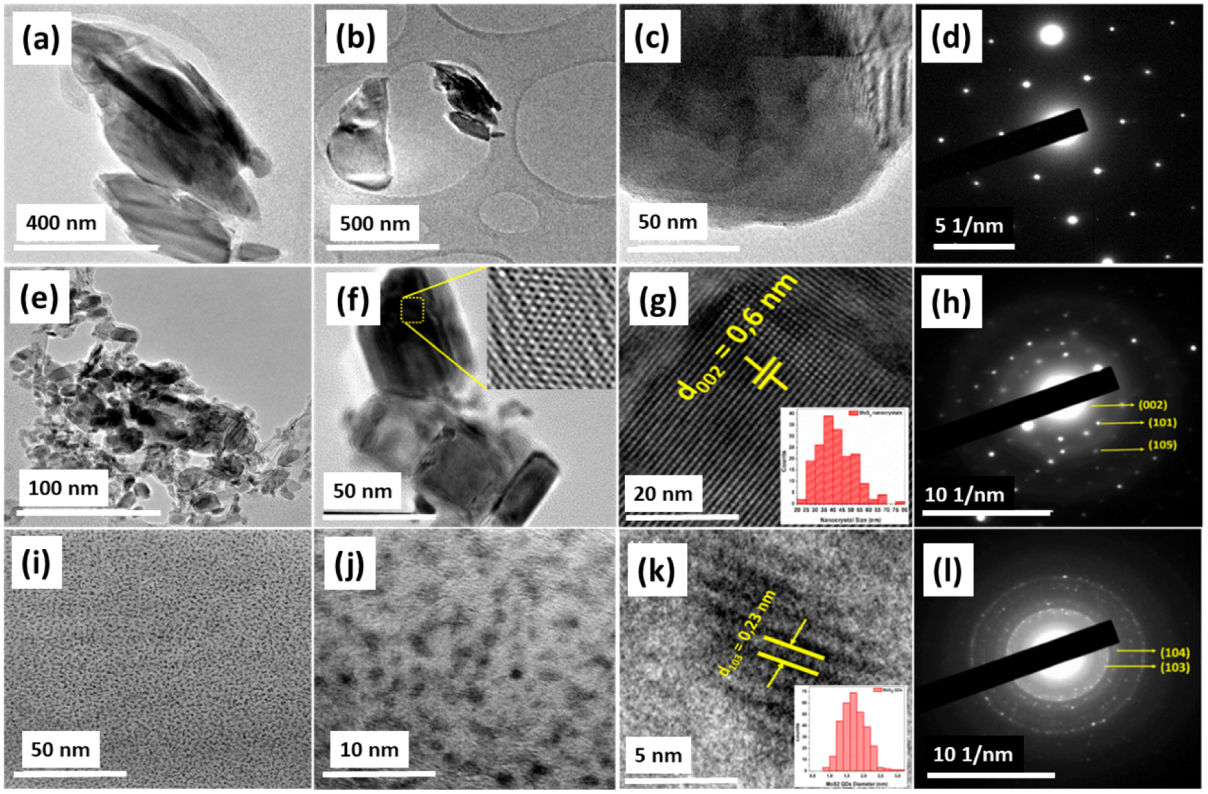

Figure 3. Different scale HRTEM images with the corresponding SAED patterns of bulk MoS_2 (a–d), MoS_2 NCs (e–h), and QDs (i–l). The histograms of the NCs and QDs sizes are respectively shown in g and k as insets.

2 for a direct allowed, n = 2 for an indirect allowed). By plotting $([F(R)h\nu])^2$ against $h\nu$, the optical band gap of the MoS_2 NCs and QDs has been determined and are shown in Figure 1f. The MoS_2 NCs have an optical band gap value of 2.82 eV and at the same time, the QDs have a wide band gap of 4.3 eV. The increment in the direct band gap energy with respect to the bulk and monolayer MoS_2 was due to the strong quantum confinement effect that led to the enhanced band gap opening.

The morphology and size of the MoS_2 NCs and QDs were analyzed by field emission scanning electron microscopy (FESEM), as shown in Figure 2. The FESEM image of bulk MoS_2 is shown in Figure 2b. It can clearly be seen that the MoS_2 NCs were mainly composed of nanoparticles that were ∼30 to 45 nm in size (Figure 2c). The MoS_2 QDs (Figure 2d) showed the uniform distribution of nanoparticles with a diameter of 1–3 nm, and the elemental mapping confirmed the presence of Mo and S atoms (Figure 2j,k).

The AFM images were obtained to characterize the morphology and the thickness of the MoS_2 NCs and QDs for further confirmation. Prior to the AFM imaging, the aqueous solution of the NCs and QDs were solution cast on 1 cm^2 pieces of Si(100) substrates. From the height profile (lines showed on Figure 2e,f) of the AFM images, the thickness of the NCs and QDs were determined and found to be in the range of ∼40 nm (Figure 2g) and 1.7–2 nm (Figure 2h), respectively, indicating that the synthesized QDs consisted out of approximately 3–4 layers. These AFM results were in reasonable agreement with those of the FESEM and high resolution transmission electron microscopy (HRTEM) images.

The morphology and size of the MoS_2 NCs and QDs were explored by HRTEM investigations. It was used to characterize the size, morphology, and lattice structure of the MoS_2 QDs and NCs. The HRTEM images of the bulk MoS_2, MoS_2 NCs, and QDs are shown in Figure 3. It shows that the as-synthesized MoS_2 NCs have a d-spacing value of 0.6 nm which represent the (002) phase of MoS_2 (Figure 3e–g). The corresponding selected area electron diffraction (SAED) pattern reflects good crystallinity with the reflections from the (002), (101), and (105) planes of the MoS_2 crystal structure (Figure 3h) corresponding to 14.8, 34.11, and 50.33°. The fast Fourier transform image (Figure 3f, inset) interprets the atomic arrangement of the MoS_2 NCs. The histogram of the NCs is shown in the inset of Figure 3g. The size distribution of the NCs is mainly around 35–40 nm. As shown in Figure 3i–l, the MoS_2 QDs have a spherical shape with a size distribution range of 1–3 nm.

The lattice fringes are shown in Figure 3k show the crystalline nature of the QDs. The measured d-spacing gave the value of 0.23 nm which corresponds to the (103) plane of the MoS_2. Likewise, the SAED pattern that was taken for the MoS_2 QDs shows the reflections of the (103) and (104) planes of MoS_2 which is well accordance with the XRD planes of MoS_2 (Figure 3l). The inset of Figure 3k depicts the histogram of the MoS_2 QDs, with the lateral size distribution with an average diameter of 1.7 nm. Especially, the size of the MoS_2 QDs reveals a prominent part distribution in the range of 1–2.5 nm, indicating that the prepared QDs were uniformly dispersed in the controllable range.

The electrochemical performance of the bulk MoS_2, MoS_2 NCs, and QDs electrodes were examined in a half-cell configuration in a 1 M Na_2SO_4 aqueous electrolyte. Figure

https://dx.doi.org/10.1021/acsomega.0c02576
ACS Omega 2021, 6, 4542–4550

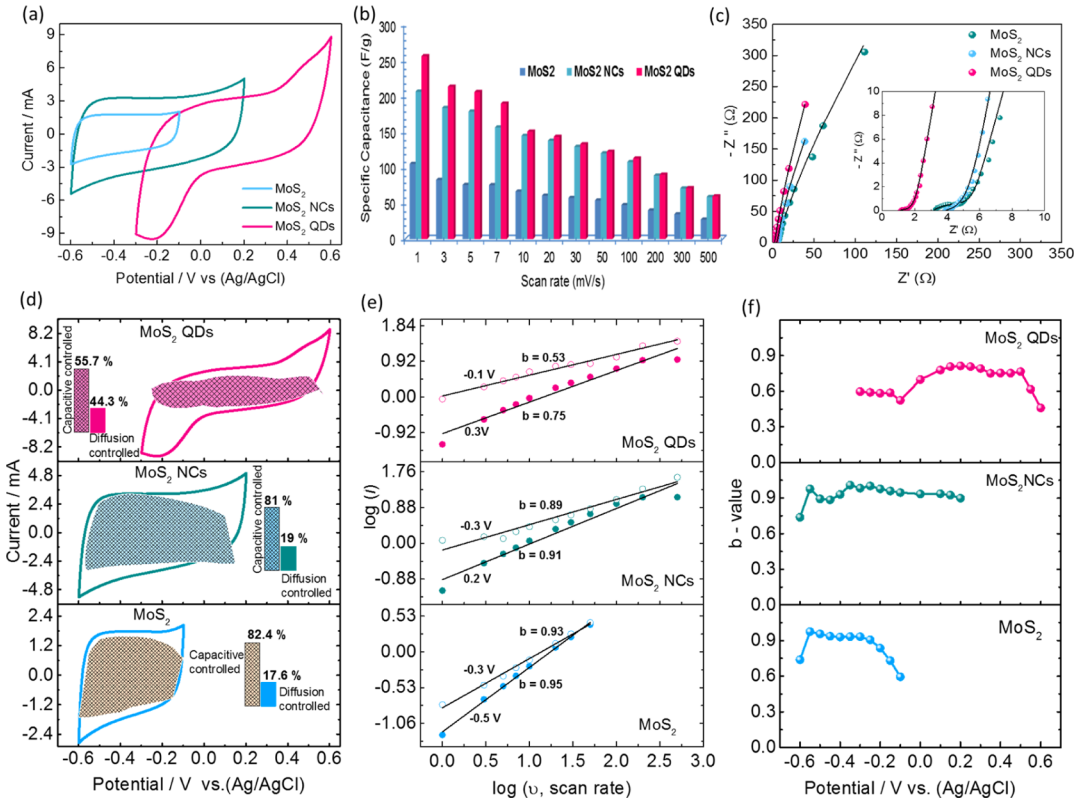

Figure 4. Electrochemical performance of bulk MoS_2, MoS_2 NCs, and QDs in a three electrode configuration measured in a 1 M Na_2SO_4 electrolyte. (a) CV curves at a scan rate of 30 mV s^{-1}, (b) calculated specific capacitances against the scan rate. (c) Nyquist plot measured by electrochemical impedance spectroscopy (EIS). (d) CV curves of bulk MoS_2, NCs, and QDs at a scan rate of 30 mV s^{-1}; shaded area indicates the contribution of a capacitive-controlled process. (e) Power law dependence of peak current at different scan rates and (f) the variation of *b*-values as a function of potentials.

4a compares the cyclic voltammetric (CV) evolutions for the electrodes at a scan rate of 30 mV s^{-1}, where the QDs electrode was found to exhibit a higher potential window than the bulk MoS_2 and the MoS_2 NCs. Despite showing the near rectangular CV curve with a significant current response of the NCs at a potential window of −0.6 to 0.2 V, the defects due to the edge and size effects of the MoS_2 QDs enhanced the active sites responsible for efficient charge accumulation at the interspace between the layers. Faradaic redox reactions occurred at its dangling edge structure and the intercalation of the electrolyte ions together with a confined pathway at a shorter diffusion length enables a significant widening of the operating potential window close to 0.9 V. The shape of the rectangular CV curve deviation for the QDs is strongly related to the intercalation of the electrolyte ions.[41,42] This can be attributed to the relationship between the structure, property and a number of effects inherent in QDs that are effectively enhanced the specific capacitance of 255 F/g at a scan rate of 1 mV s^{-1} (206 F/g for NCs and 105 F/g for bulk MoS_2), and retained its initial capacitance of ∼44% (∼113 F/g), Figure 5b, at a scan rate of 100 mV s^{-1} and 56 F/g at a scan rate of 500 mV s^{-1} indicating the excellent rate capability as compared to NCs and bulk MoS_2 electrodes. Furthermore, in order to confirm the enhanced ion propagations in the QDs, the electrochemical impedance analysis was performed to extract the solution resistance (R_s) and charge transfer resistance (R_{ct}). Figure 4c shows the Nyquist plot for all electrodes in the half-cell configuration which revealed that the QDs exhibited both a low R_s value of 0.9 Ω and R_{ct} value of 1.72 Ω with a linear curve which is typical of a SC behaviour in the low frequency region. In comparison the NCs values were R_s = 3.85 Ω and R_{ct} = 4.18 Ω and for bulk MoS_2 the values were R_s = 3.23 Ω and R_{ct} = 4.57 Ω. This demonstrates that there was an improvement in the electronic conductivity and redox kinetics for the QDs.

In order to distinguish and quantify the total stored charge in the QDs the three contributions: faradaic fast charge-transfer process on the surface, the non-faradaic contribution from the double layer adsorption, and diffusion-controlled faradaic process were evaluated.[43,44] The contributions can be separated by using the power law relationship with measured current (i) response from cyclic voltammetry and different scan rate (ν).

$$i = a\nu^b \tag{4}$$

where, "*a*" and "*b*" are adjustable parameters. The measured slope "*b*" value indicates the predominant contributions if b = 0.5 it is mainly by a diffusion-controlled process and if b = 1 it is dominated by a capacitive process. Figure 4e,f clearly indicates that the QDs showed different *b*-values, b = 0.53 at −0.1 V and 0.75 at 0.3 V when compared to the NCs (b = ∼0.9) and bulk MoS_2 (b = ∼0.94), inferring the current response is mainly due to the capacitive process for NCs and bulk MoS_2 electrodes. A significant contribution from the intercalation process by rapid insertion and extraction of the electrolyte ions may be attributed to the increase in the number of the edge atoms in the QDs, which are responsible for widening the potential window and the enhancement of

https://dx.doi.org/10.1021/acsomega.0c02576
ACS Omega 2021, 6, 4542−4550

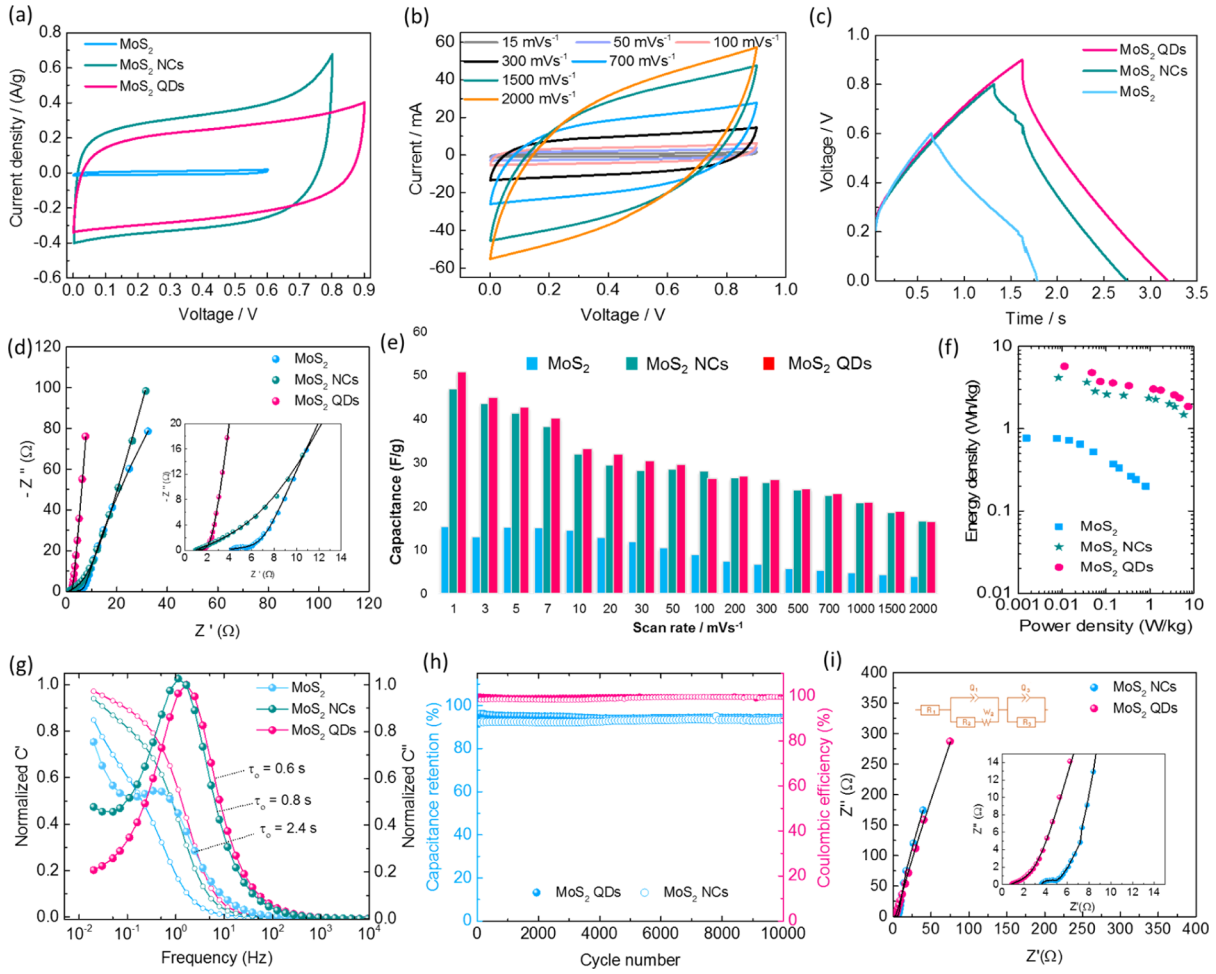

Figure 5. Electrochemical performance of symmetric aqueous SCs in 1 M Na_2SO_4 electrolyte. (a) CV curves of the symmetric device for the bulk MoS_2, NCs and QDs, (b) CV curves of QDs at different scan rates, (c) galvanostatic charge−discharge profile at 1 A/g, (d) Nyquist profile for all devices at room temperature, (e) device capacitance calculated from CV curves at different scan rates, (f) Ragone profile for energy and power density of the device, (g) frequency dependence of the real and imaginary parts of capacitance, (h) cycle stability test of NCs and QDs symmetric devices at a current density of 0.5 A/g, and (i) Nyquist profiles for NCs and QDs devices tested after 10,000 consecutive cycles, inset showed the expanded view and RC circuit used for fitting.

overall capacitance in accordance with the *b*-values of the QDs. The capacitive contribution to the overall current response can be separated by

$$i(V) = k_1\nu + k_2\nu^{1/2} \tag{5}$$

where ν is the scan rate (mV/s), $k_1\nu$ and $k_2\nu^{1/2}$ are the obtained currents from capacitive contribution and diffusion-controlled faradaic contribution, respectively.

$$\frac{i(V)}{\nu^{1/2}} = k_1\nu^{1/2} + k_2 \tag{6}$$

A linear plot can be obtained by modifying the eqs 5 and 6, and k_1 and k_2 can be derived from $i(V)/\nu^{1/2}$ versus $\nu^{1/2}$ with different scan rates.

Figure 4d describes the CV profiles of the bulk MoS_2, NCs and QDs at a scan rate of 30 mV s^{-1}. The shaded area indicates the contribution of the capacitive-controlled process. The QDs possess ∼44% (∼18% for NCs) of the diffusion-controlled that is intercalation process contribution to the overall capacitance. The increase in the intercalation process established that the electrodes possess in the order of bulk MoS_2 > NCs > QDs owing to the increasing number of edge atoms and confinement effects.

Figure 5a compares the CV characteristics of symmetric devices of the bulk MoS_2, NCs and QDs in 1 M Na_2SO_4 aqueous solution. The CV characteristics of the QDs show better performance than the bulk MoS_2 and the MoS_2 NCs electrodes. Despite the NCs showing a higher current response, the improved operating voltage window with the QDs electrodes is an advantage with a high energy density of 5.7 W h kg^{-1} (0.77 and 4.2 W h/kg for bulk MoS_2 and MoS_2 NCs) at a scan rate of 1 mV s^{-1} and a power density of 7.4 W/kg (& 0.8 & 5.9 W/kg for bulk MoS_2 and MoS_2 NCs) at a scan rate of 2 V s^{-1} (Figure 5f). The comparison of energy density with MoS_2 QDs with that of the reported values is tabulated in Table S2. The higher current response of the NCs may be attributed to the enhanced surface activity with the electrolyte ions. However, the space to accommodate more ions is limited due to the inaccessible regions, suggesting a device is fully charged at 0.8 V.[41,42,45] In contrast to NCs, the QDs have inherent surface defects consisting of more edge atoms together with shorter conductive pathways as QDs are close enough to ensure that the interactions with ions are strongly responsible for stipulating the redox kinetics and surface

https://dx.doi.org/10.1021/acsomega.0c02576
ACS Omega 2021, 6, 4542−4550

reactions.[26,29,30] Hence, the voltage window is widened to 0.9 V of the QDs symmetric device (Figure 5c). The CV response at different scan rates ranging from 1 mV to 2 V for the QDs (Figure 5b) exhibited excellent rate capability with an initial device capacitance of 51 F/g (~47 F/g for NCs and 15 F/g for bulk MoS_2) (Figure 5e) and retained ~50% (24.5 F/g) of its initial capacitance at a scan rate of 500 mV s^{-1} and ~34% at a scan rate of 2 V. From the electrochemical impedance analysis, it is evident that the high rate capability of QDs with its low response time of ~0.6 s and low R_{ct} value of 1.92 Ω (Figure 5d,g) compared to the NCs (0.8 s), bulk MoS_2 (2.4 s) and graphene (~10 s). Figure 5h describes the cycle stability test of the QDs and the NCs devices over 10,000 consecutive cycles at a current density of 0.5 A/g, which demonstrates excellent cycle life with the capacitance retention of ~94% for the QDs and 91% for the NCs upon 10k cycles with 100% Coulombic efficiency. The cycle stability performance further strengthened by the EIS data analyzed after prolonged charge−discharge cycling for the QDs and the NCs showed almost linear curves with little resistance gain (Figure 5i), confirming the structural integrity of the luminescent QDs.

CONCLUSIONS

A uniform ~2 nm size of MoS_2 QDs were successfully synthesized by LACVD and used as an electrode material for SCs. The as-synthesized QDs exhibited an extended electrochemical potential window of 0.9 V with a specific capacitance value of 255 F/g. A shorter conductive pathway of QDs consisting with more number of edge atoms ensure the efficient and enhanced the redox kinetics and surface reactions. The symmetric device fabricated with MoS_2 QDs showed a remarkable device capacitance value of 50 F/g at a scan rate of 1 mV s^{-1} with an energy density of ~5.7 W h kg^{-1}. The device exhibited long cycle stability of 10,000 consecutive cycles with ~95% capacitance retention. This work opens the door for scalable production of uniform QDs with effective active sites as an excellent electrode material for SC devices.

EXPERIMENTAL PROCEDURE

Chemicals. Bulk MoS_2 powder (Sigma-Aldrich, 99% purity, 2H) <2 μm average size, 1% polyvinyl alcohol (Sigma-Aldrich, M_w 89,000−98,000), and 1% gold(III) chloride ($AuCl_2$) were thoroughly mixed. The mixture was hard-pressed into a pellet using a piston and sleeve system, while kept in a vacuum oven at a temperature of 120 °C for 24 h to obtain a MoS_2 target with a thickness of 10 mm and a diameter of 20 mm.

Synthesis of MoS_2 NCs and QDs. In the LACVD setup, the quartz-tube (QT) was first evacuated to a base pressure of 2.7×10^{-2} mbar. A *q*-switched Nd:YAG (Spectra-Physics GCR-4) laser operating at 1064 and 532 nm temporarily and spatially separated by the path difference of 20 ns and 10 Hz pulse repetition rate was used to ablate the target. The first and second harmonic (1064 and 532 nm) energies were 465 and 512 mJ per pulse. An anti-reflected coated lens of focal length 1500 mm was used to focus the beams onto the target surface. The focused beams had a spot size of approximately 3 mm in diameter. In order to minimize refection of the laser beams at the entrance of the quartz tube, a window fixed at the Brewster angle was used. The focused beams at the target surface have approximate energy densities of 7.24 and 6.58 J cm^{-2} at 1064 and 533 nm, respectively. The laser-ablation process occurred at an argon pressure of 400 Torr and flow rate of 200 sccm within the closed QT. The temperature of the furnace was ramped to 700 °C (NCs) and 900 °C (QDs). The small inner QT placed inside the tube furnace allowed a laminar flow of Ar gas toward the target. The Ar gas functions as the carrier gas as well aid in the promotion of self-assembly of the dissociated Mo and S ions/atoms. The laser beams raster the target to uniformly ablate the target surface. The duration of the ablation process was 40 min. The energy from the laser beams was absorbed in the target prior to any significant thermal-conduction as well as plasma-expansion could occur. Thus, the laser beam generates results in thermal conduction on the target surface to form plasma at a particular temperature and pressure (schematic diagram in Figure 2a). This laser-induced plasma contains vaporized elements of the target in different stages of ionization and together form a plasma. As the outwardly expanding plasma cools, Mo and S bond to MoS_2 as molecular vapor and upon further cooling form MoS_2 nanostructures (NCs and QDs) depending on the temperature maintained during the reaction period (700 and 900 °C).

Materials Characterization. The crystallinity and phase purity of the as-synthesized MoS_2, QDs and NCs were studied by powder XRD (PXRD) patterns using a Bruker D8 ADVANCE with Cu Kα radiation (λ = 1.5406 Å). The PXRD patterns were recorded between 10 and 60° at increments of 0.02°. Raman spectroscopy was used to identify the vibrational modes of the MoS_2, QDs, and NCs with a Jobin Yvon LabRAM HR800 spectrograph utilizing visible laser (λ = 514 nm) radiation. The morphologies were obtained with a FESEM (Zeiss ultra plus) and a HRTEM using a JEOL-TEM 2100 working at an accelerating voltage of 200 kV. A carbon coated copper grids were used as the substrates for the HRTEM measurements. The optical properties of the materials were characterized by using an ultraviolet−visible−near infrared (UV−vis−NIR) with a UV−vis−NIR-Shimadzu 3600 spectrograph, and PL spectroscopy was performed on a PerkinElmer LS-55 spectrograph. The electrical properties were measured by using a Keithley 2450 voltage source meter equipped with a Jandel four-point probe with probes spacing of 1 mm.

Electrochemical Measurements. All electrochemical analysis on the QDs, NCs, and pristine MoS_2 were carried out on a Bio-Logic VMP3@EC-LAB 10.40 at room temperature. The slurry mixture was well grinded and dispersed in an ultrasonication method for 15 min which prevents the agglomeration. Finally, the composite electrode was prepared by spreading a slurry mixture of the active material, carbon black, and poly(vinylidene fluoride) (80:15:5 weight ratio) on a piece of nickel foam, and then, it was dried in a vacuum oven at 120 °C for 12 h. In a typical three-electrode system, the obtained composite electrode was used as the working electrode, platinum mesh and Ag/AgCl (KCl) were used as counter and reference electrodes, respectively, and 1 M Na_2SO_4 aqueous solution as the electrolyte. Cyclic voltammograms were carried out in a potential range of 0−0.9 V at different scan rates from 5 to 2000 mV s^{-1}. The galvanostatic charge−discharge studies were performed within the voltage window of 0−0.9 V at different current densities ranging from 1 to 5 A g^{-1}. EIS measurements were carried out in the frequency ranging from 10 kHz to 10 mHz at the open circuit voltage with an AC voltage amplitude of 1.5 mV. A symmetric SC (2-electrode) was fabricated with the QDs, NCs, and MoS_2 electrodes on both sides and performed in a 1 M Na_2SO_4 aqueous solution as the electrolyte. The specific capacitance

https://dx.doi.org/10.1021/acsomega.0c02576
ACS Omega 2021, 6, 4542−4550

(C_{sp}), device capacitance, specific power density (P), and energy density (E_{sp}) were calculated from the CV curves using the established following equations.[9,46]

$$C_g = \frac{1}{Vmv}\int i\,dV \tag{7}$$

$$C_{sp}\ (\mathrm{F/g}) = \frac{4C}{m} \tag{8}$$

$$E\ (\mathrm{W\,h/kg}) = \frac{CV^2}{2m} \tag{9}$$

where i (A) is the applied current, ΔV (V)/Δt (s) the slope of the discharge curve, and m (g) the total mass of both electrodes, C (F) the calculated capacitance, V (V) is the maximum voltage obtained during charge, and R_s is the equivalent series resistance.

■ ASSOCIATED CONTENT

Supporting Information

The Supporting Information is available free of charge at https://pubs.acs.org/doi/10.1021/acsomega.0c02576.

Comparison of electrical conductivity of MoS_2, MoS_2 NCs, and MoS_2 QDs and comparison of energy density with MoS_2 QDs with that of the reported values (PDF)

■ AUTHOR INFORMATION

Corresponding Authors

Kumar Raju − *Energy Centre, Council for Scientific and Industrial Research (CSIR), Pretoria 0001, South Africa;* orcid.org/0000-0002-6143-0720; Email: kraju@csir.co.za

Mathew K. Moodley − *Discipline of Physics, School of Chemistry and Physics, University of KwaZulu-Natal, Durban 4000, South Africa;* orcid.org/0000-0002-4089-7380; Email: Moodleymk@ukzn.ac.za

Authors

Sarojini Jeeva Panchu − *Discipline of Physics, School of Chemistry and Physics, University of KwaZulu-Natal, Durban 4000, South Africa; Department of Physics, University of the Free State, Bloemfontein 9300, South Africa*

Hendrik C. Swart − *Department of Physics, University of the Free State, Bloemfontein 9300, South Africa;* orcid.org/0000-0001-5233-0130

Bharatiraja Chokkalingam − *Department of Electrical and Electronics Engineering, SRM Institute of Science and Technology, Kattankulathur 603203, India*

Malik Maaza − *Nanosciences African Network (NANOAFNET), iThemba LABS-National Research Foundation, 7129 Somerset West, South Africa*

Mohamed Henini − *School of Physics and Astronomy, Nottingham Nanotechnology and Nanoscience Center, University of Nottingham, Nottingham NG7 2RD, U.K.*

Complete contact information is available at: https://pubs.acs.org/10.1021/acsomega.0c02576

Notes

The authors declare no competing financial interest.

■ ACKNOWLEDGMENTS

S.J.P. grateful to University of KwaZulu Natal, the National Research Foundation (NRF) South Africa for the Free Standing Doctoral Grant (grant UID: 112896). We are grateful to the Microscopy and Microanalysis Unit (MMU, University of KwaZulu-Natal).

■ REFERENCES

(1) Simon, P.; Gogotsi, Y. Materials for Electrochemical Capacitors. *Nat. Mater.* **2008**, *7*, 845−854.

(2) Miller, J. R.; Simon, P.; Patrice, S. Electrochemical Capacitors for Energy Management. *Science* **2008**, *321*, 651−652.

(3) Lukatskaya, M. R.; Dunn, B.; Gogotsi, Y. Multidimensional Materials and Device Architectures for Future Hybrid Energy Storage. *Nat. Commun.* **2016**, *7*, 12647.

(4) Wang, G.; Zhang, L.; Zhang, J. A Review of Electrode Materials for Electrochemical Supercapacitors. *Chem. Soc. Rev.* **2012**, *41*, 797−828.

(5) Xu, Y.; Lin, Z.; Zhong, X.; Huang, X.; Weiss, N. O.; Huang, Y.; Duan, X. Holey Graphene Frameworks for Highly Efficient Capacitive Energy Storage. *Nat. Commun.* **2014**, *5*, 4554.

(6) Wang, Q.; Yan, J.; Fan, Z. Carbon Materials for High Volumetric Performance Supercapacitors: Design, Progress, Challenges and Opportunities. *Energy Environ. Sci.* **2016**, *9*, 729−762.

(7) Lukatskaya, M. R.; Kota, S.; Lin, Z.; Zhao, M.-Q.; Shpigel, N.; Levi, M. D.; Halim, J.; Taberna, P.-L.; Barsoum, M. W.; Simon, P.; et al. Ultra-High-Rate Pseudocapacitive Energy Storage in Two-Dimensional Transition Metal Carbides. *Nat. Energy* **2017**, *2*, 17105.

(8) Acerce, M.; Voiry, D.; Chhowalla, M. Metallic 1T Phase MoS2 Nanosheets as Supercapacitor Electrode Materials. *Nat. Nanotechnol.* **2015**, *10*, 313−318.

(9) Raju, K.; Han, H.; Velusamy, D. B.; Jiang, Q.; Yang, H.; Nkosi, F. P.; Palaniyandy, N.; Makgopa, K.; Bo, Z.; Ozoemena, K. I. Rational Design of 2D Manganese Phosphate Hydrate Nanosheets as Pseudocapacitive Electrodes. *ACS Energy Lett.* **2020**, *5*, 23−30.

(10) Jiao, Y.; Hafez, A. M.; Cao, D.; Mukhopadhyay, A.; Ma, Y.; Zhu, H. Metallic MoS2 for High Performance Energy Storage and Energy Conversion. *Small* **2018**, *14*, 1800640.

(11) Zhang, W.-J.; Huang, K.-J. A Review of Recent Progress in Molybdenum Disulfide-Based Supercapacitors and Batteries. *Inorg. Chem. Front.* **2017**, *4*, 1602−1620.

(12) Pomerantseva, E.; Bonaccorso, F.; Feng, X.; Cui, Y.; Gogotsi, Y. Energy Storage: The Future Enabled by Nanomaterials. *Science* **2019**, *366*, No. eaan8285.

(13) Zhang, Y.; Zhou, Q.; Zhu, J.; Yan, Q.; Dou, S. X.; Sun, W. Nanostructured Metal Chalcogenides for Energy Storage and Electrocatalysis. *Adv. Funct. Mater.* **2017**, *27*, 1702317.

(14) Yu, Z.; Tetard, L.; Zhai, L.; Thomas, J. Supercapacitor Electrode Materials: Nanostructures from 0 to 3 Dimensions. *Energy Environ. Sci.* **2015**, *8*, 702−730.

(15) Kumar, K. S.; Choudhary, N.; Jung, Y.; Thomas, J. Recent Advances in Two-Dimensional Nanomaterials for Supercapacitor Electrode Applications. *ACS Energy Lett.* **2018**, *3*, 482−495.

(16) Zhou, C.; Wang, J.; Yan, X.; Yuan, X.; Wang, D.; Zhu, Y.; Cheng, X. Vertical MoS_2 Nanosheets Arrays on Carbon Cloth as Binder-Free and Flexible Electrode for High-Performance All-Solid-State Symmetric Supercapacitor. *Ceram. Int.* **2019**, *45*, 21534−21543.

(17) Chen, M.; Dai, Y.; Wang, J.; Wang, Q.; Wang, Y.; Cheng, X.; Yan, X. Smart Combination of Three-Dimensional-Flower-like MoS_2 nanospheres/Interconnected Carbon Nanotubes for Application in Supercapacitor with Enhanced Electrochemical Performance. *J. Alloys Compd.* **2017**, *696*, 900−906.

(18) Wang, J.; Zhou, C.; Yan, X.; Wang, Q.; Sha, D.; Pan, J.; Cheng, X. Hydrothermal Synthesis of Hierarchical Nanocomposite Assembled by Bi_2S_3 Nanorods and MoS_2 Nanosheets with Improved Electrochemical Performance. *J. Mater. Sci. Mater. Electron.* **2019**, *30*, 6633−6642.

(19) Wang, J.; Chen, M.; Yan, X.; Zhou, C.; Wang, Q.; Wang, D.; Yuan, X.; Pan, J.; Cheng, X. A Facile One-Step Hydrothermal Synthesis of Carbon−MoS_2 Yolk−Shell Hierarchical Microspheres with Excellent Electrochemical Cycling Stability. *J. Appl. Electrochem.* **2018**, *48*, 509−518.
(20) Chen, M.; Wang, J.; Yan, X.; Ren, J.; Dai, Y.; Wang, Q.; Wang, Y.; Cheng, X. Flower-like Molybdenum Disulfide Nanosheets Grown on Carbon Nanosheets to Form Nanocomposites: Novel Structure and Excellent Electrochemical Performance. *J. Alloys Compd.* **2017**, *722*, 250−258.
(21) Sun, T.; Li, Z.; Liu, X.; Ma, L.; Wang, J.; Yang, S. Oxygen-Incorporated MoS_2 Microspheres with Tunable Interiors as Novel Electrode Materials for Supercapacitors. *J. Power Sources* **2017**, *352*, 135−142.
(22) Acerce, M.; Voiry, D.; Chhowalla, M. Metallic 1T Phase MoS_2 Nanosheets as Supercapacitor Electrode Materials. *Nat. Nanotechnol.* **2015**, *10*, 313−318.
(23) Wei, S.; Zhou, R.; Wang, G. Enhanced Electrochemical Performance of Self-Assembled Nanoflowers of MoS_2 Nanosheets as Supercapacitor Electrode Materials. *ACS Omega* **2019**, *4*, 15780.
(24) Ghasemi, F.; Jalali, M.; Abdollahi, A.; Mohammadi, S.; Sanaee, Z.; Mohajerzadeh, S. A High Performance Supercapacitor Based on Decoration of MoS_2/Reduced Graphene Oxide with NiO Nanoparticles. *RSC Adv.* **2017**, *7*, 52772−52781.
(25) Wang, N.; Pan, Q.; Yang, X.; Zhu, H.; Ding, G.; Jia, Z.; Wu, Y.; Zhao, L. High Performance Asymmetric Supercapacitor Based on Ni_xS_y/MoS_2 Nanoparticles. *ACS Appl. Nano Mater.* **2019**, *2*, 4910−4920.
(26) Choudhary, N.; Patel, M.; Ho, Y.-H.; Dahotre, N. B.; Lee, W.; Hwang, J. Y.; Choi, W. Directly Deposited MoS2 Thin Film Electrodes for High Performance Supercapacitors. *J. Mater. Chem. A* **2015**, *3*, 24049−24054.
(27) Das, S.; Ghosh, R.; Mandal, D.; Nandi, A. K. Self-Assembled Nanostructured MoS2 Quantum Dot Polyaniline Hybrid Gels for High Performance Solid State Flexible Supercapacitors. *ACS Appl. Energy Mater.* **2019**, *2*, 6642−6654.
(28) Li, F.; Li, J.; Cao, Z.; Lin, X.; Li, X.; Fang, Y.; An, X.; Fu, Y.; Jin, J.; Li, R. MoS2 Quantum Dot Decorated RGO: A Designed Electrocatalyst with High Active Site Density for the Hydrogen Evolution Reaction. *J. Mater. Chem. A* **2015**, *3*, 21772−21778.
(29) Li, B.; Jiang, L.; Li, X.; Ran, P.; Zuo, P.; Wang, A.; Qu, L.; Zhao, Y.; Cheng, Z.; Lu, Y. Preparation of Monolayer MoS2 Quantum Dots Using Temporally Shaped Femtosecond Laser Ablation of Bulk MoS2 Targets in Water. *Sci. Rep.* **2017**, *7*, 11182.
(30) Yang, Y.; Fei, H.; Ruan, G.; Xiang, C.; Tour, J. M. Edge-Oriented MoS2 Nanoporous Films as Flexible Electrodes for Hydrogen Evolution Reactions and Supercapacitor Devices. *Adv. Mater.* **2014**, *26*, 8163−8168.
(31) Yan, Y.; Zhang, C.; Gu, W.; Ding, C.; Li, X.; Xian, Y. Facile Synthesis of Water-Soluble WS 2 Quantum Dots for Turn-On Fluorescent Measurement of Lipoic Acid. *J. Phys. Chem. C* **2016**, *120*, 12170−12177.
(32) Ha, H. D.; Han, D. J.; Choi, J. S.; Park, M.; Seo, T. S. Dual Role of Blue Luminescent MoS 2 Quantum Dots in Fluorescence Resonance Energy Transfer Phenomenon. *Small* **2014**, *10*, 3858−3862.
(33) Gopalakrishnan, D.; Damien, D.; Shaijumon, M. M. MoS2 Quantum Dot-Interspersed Exfoliated MoS2 Nanosheets. *ACS Nano* **2014**, *8*, 5297−5303.
(34) Ren, X.; Pang, L.; Zhang, Y.; Ren, X.; Fan, H.; Liu, S. One-Step Hydrothermal Synthesis of Monolayer MoS_2 Quantum Dots for Highly Efficient Electrocatalytic Hydrogen Evolution. *J. Mater. Chem. A* **2015**, *3*, 10693−10697.
(35) Gopalakrishnan, D.; Damien, Y.-W.; Li, B.; Gullappalli, H.; Pillai, V. K.; Ajayan, P. M.; Shaijumon, M. M. Electrochemical Synthesis of Luminescent MoS2 Quantum Dots. *Chem. Commun.* **2015**, *51*, 6293−6296.
(36) Li, B. L.; Chen, L. X.; Zou, H. L.; Lei, J. L.; Luo, H. Q.; Li, N. B. Electrochemically Induced Fenton Reaction of Few-Layer MoS2 Nanosheets: Preparation of Luminescent Quantum Dots via a Transition of Nanoporous Morphology. *Nanoscale* **2014**, *6*, 9831−9838.
(37) Pan, H.; Zhang, Y. W. Edge-Dependent Structural, Electronic and Magnetic Properties of MoS2 Nanoribbons. *J. Mater. Chem.* **2012**, *22*, 7280−7290.
(38) Alkis, S.; Öztaş, T.; Aygün, L. E.; Bozkurt, F.; Okyay, A. K.; Ortaç, B. Thin Film MoS_2 Nanocrystal Based Ultraviolet Photodetector. *Opt. Express* **2012**, *20*, 21815.
(39) Li, H.; Lu, G.; Yin, Z.; He, Q.; Li, H.; Zhang, Q.; Zhang, H. Optical Identification of Single- and Few-Layer MoS 2 Sheets. *Small* **2012**, *8*, 682−686.
(40) Siddiqui, G. U.; Ali, J.; Choi, K. H.; Jang, Y.; Lee, K. Fabrication of Blue Luminescent MoS2 Quantum Dots by Wet Grinding Assisted Co-Solvent Sonication. *J. Lumin.* **2016**, *169*, 342−347.
(41) Sarkar, D.; Das, D.; Das, S.; Kumar, A.; Patil, S.; Nanda, K. K.; Sarma, D. D.; Shukla, A. Expanding Interlayer Spacing in MoS2 for Realizing an Advanced Supercapacitor. *ACS Energy Lett.* **2019**, *4*, 1602−1609.
(42) Li, J.; An, L.; Li, H.; Sun, J.; Shuck, C.; Wang, X.; Shao, Y.; Li, Y.; Zhang, Q.; Wang, H. Tunable Stable Operating Potential Window for High-Voltage Aqueous Supercapacitors. *Nano Energy* **2019**, *63*, 103848.
(43) Wang, R.; Wang, S.; Peng, X.; Zhang, Y.; Jin, D.; Chu, P. K.; Zhang, L. Elucidating the Intercalation Pseudocapacitance Mechanism of MoS2-Carbon Monolayer Interoverlapped Superstructure: Toward High-Performance Sodium-Ion-Based Hybrid Supercapacitor. *ACS Appl. Mater. Interfaces* **2017**, *9*, 32745−32755.
(44) Jiang, Q.; Kurra, N.; Alhabeb, M.; Gogotsi, Y.; Alshareef, H. N. All Pseudocapacitive MXene-RuO_2 Asymmetric Supercapacitors. *Adv. Energy Mater.* **2018**, *8*, 1703043.
(45) Khawula, T. N. Y.; Raju, K.; Franklyn, P. J.; Sigalas, I.; Ozoemena, K. I. Symmetric Pseudocapacitors Based on Molybdenum Disulfide (MoS2)-Modified Carbon Nanospheres: Correlating Physicochemistry and Synergistic Interaction on Energy Storage. *J. Mater. Chem. A* **2016**, *4*, 6411−6425.
(46) Raju, K.; Ozoemena, K. I. Hierarchical One-Dimensional Ammonium Nickel Phosphate Microrods for High-Performance Pseudocapacitors. *Sci. Rep.* **2015**, *5*, 17629.

https://dx.doi.org/10.1021/acsomega.0c02576
ACS Omega 2021, 6, 4542−4550